Mon. Not. R. Astron. Soc. **000**, 1–13 (2006) Printed 25 December 2006 (MN LATEX style file v2.2)

Jet radio emission in Cygnus X-1 and its orbital modulation

Anna Szostek⋆ and Andrzej A. Zdziarski⋆
Centrum Astronomiczne im. M. Kopernika, Bartycka 18, 00-716 Warszawa, Poland

arXiv:astro-ph/0610017v3 22 Dec 2006

Accepted . Received ; in original form

ABSTRACT

We present results of our detailed theoretical study of the observed orbital modulation of the radio emission in Cyg X-1. The modulation occurs due to free-free absorption in the wind from the companion star varying with the orbital phase, and our results put strong constraints on the spatial distribution of the jet radio emission at the frequencies of 2–15 GHz. A crucial role in enhancing the asymmetry of the wind absorption suffered by the jet emission is played by the irradiation by X-rays emitted in the vicinity of the black hole. This increases the wind temperature by more than order of magnitude with respect to that of the wind of an isolated supergiant. The observed phase lags of the minima of the radio emission with respect to the spectroscopic zero phase strongly imply the bulk of the mass of the jet is nonrelativistic ($\sim 5\times 10^8$ cm s^{-1}) within the jet core. The jet can, however, become relativistic outside the core. Also, the jet can have a two-component structure, being slow on the outside and fast inside, in which case its synchrotron-emitting part may be relativistic already in the core. We also consider the observed superorbital modulation of the radio emission (with the period of $\sim$150 d) and find it can be explained by a jet precession both causing variable wind absorption and changing the jet Doppler factor. Finally, we consider the case of Cyg X-3, and show that its lack of observable orbital radio modulation (in spite of strong modulation of X-rays) is explained by that system being both much more compact and much more luminous than Cyg X-1.

Key words: acceleration of particles – binaries: general – radio continuum: stars – stars: individual: Cyg X-1 – stars: individual: HDE 226868 – stars: individual: Cyg X-3

1 INTRODUCTION

Cyg X-1 is a high-mass X-ray binary with the orbital period of $P = 5.6$ d (Gies & Bolton 1982), containing a black hole (Bolton 1972; Webster & Murdin 1972) and the O9.7 Iab supergiant HDE 226868 primary (Walborn 1973). Although the primary nearly fills the Roche lobe, accretion is via a stellar wind (Gies & Bolton 1986a; Gies et al. 2003). Observations of optical lines indicate that the wind departs from the spherical symmetry by being focused towards the compact object. Still, only a few percent of the wind is accreted.

The orbital period has been detected in all energy bands where the source was detected. X-ray modulation in the hard spectral state has the form of broad intensity dips accompanied by spectral hardening centred on the superior conjunction of the X-ray source, i.e., when it is behind the primary (e.g., Priedhorsky, Brandt & Lund 1995; Wen et al. 1999; Lachowicz et al. 2006, hereafter L06). The dip is a result of bound-free absorption by the wind (Wen et al. 1999). Periodic changes in equivalent widths of UV absorption lines are due to the orbital motion of a highly ionized, X-ray irradiated, region of the stellar wind. In the superior conjunction, the equivalent widths achieve the maximal values (Treves et al. 1980). In the visual band, the orbital period is seen in radial velocity variations of absorption and emission lines (e.g., Bolton 1975) and in ellipsoidal variations (Walker 1972).

The radio emission of Cyg X-1 is most likely due to the synchrotron process in a jet, whose velocity has been claimed to be mildly relativistic, $\sim 0.6c$ (Stirling et al. 2001, hereafter S01; Gleissner et al. 2004). It has a flat (in the energy flux, F_ν) spectrum at $F_\nu \sim$ 10–20 mJy in the X-ray hard spectral state (see, e.g., Zdziarski et al. 2002 for a review of the X-ray states of Cyg X-1), with no detection of either low or high frequency cut-off between 2.2 and 220 GHz (Fender et al. 2000).

Orbital periodicity of the radio emission was discovered by Han (1993). However, more insight in it was possible thanks to long term radio monitoring of Cyg X-1 by the

⋆ E-mail: asz@camk.edu.pl, aaz@camk.edu.pl

© 2006 RAS

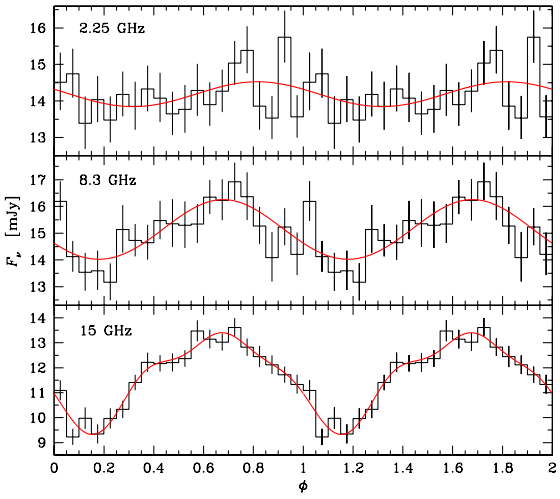

Figure 1. The average hard-state orbital modulation profiles at 2.25, 8.3 and 15 GHz (L06). The curves give the best fits with one (2.25, 8.3 GHz) and three (15 GHz) harmonics (L06). Two orbital periods are shown for clarity.

Ryle Telescope at the Mullard Radio Astronomy Observatory at 15 GHz and the Green Bank Interferometer at 2.25 and 8.3 GHz (Pooley, Fender & Brocksopp 1999; L06). It was found that the total modulation depth *in the hard state* increases with the frequency, from ∼0.03 at 2.25 GHz to ∼0.3 at 15 GHz, and that there is a time lag of the minimum of the modulation with respect to the superior conjunction decreasing with the frequency, from ∼0.3 of the orbital period at 2.25 GHz to ∼0.15 of it at 15 GHz. In the soft state, the orbital modulation takes place as well (L06), but constraints on it are much weaker, due to the much lower on average but flaring flux (Fender et al. 2006; L06).

We would like to point out that an orbital periodicity of radio emission is a rare phenomenon in X-ray binaries. It appears to be seen in only two other systems, LSI +61°303 (Taylor & Gregory 1982) and Cir X-1 (Whelan et al. 1977). Both of them are of rather different nature than Cyg X-1. Although their compact objects orbit around stars undergoing heavy mass loss (as in Cyg X-1), the orbits are wide and highly eccentric. During the periastron passage, the accretion rate onto the compact object is greatly enhanced and both the X-ray and radio fluxes increase (e.g., Coe et al. 1983; Marti & Paredes 1995; Haynes, Lerche & Murdin 1980). On the other hand, this is certainly not the case in Cyg X-1, in which the orbit is circular (Brocksopp et al. 1999b), and the orbital separation is similar to the diameter of the primary. Thus, the nature of the orbital modulation of its radio emission has to be different.

The process likely to be responsible for the modulation of the radio emission has been identified by Brocksopp, Fender & Pooley (2002, hereafter BFP02). They proposed it is free-free absorption in the stellar wind of the primary. It is then analogous to the X-ray modulation, except for the absorption being free-free rather than bound-free.

Unfortunately, although the work of BFP02 generally explains the origin of the radio modulation, it is plagued by a number of errors (as noticed by L06). Due to those errors, their results are generally incorrect. For example, errors in the equations and the numerical code used lead to the result that the fractional depth of the modulation *decreases* with the increasing inclination. This result is rather counterintuitive, as the system is fully symmetric for a face-on observer and most asymmetric for an edge-on one, and it is indeed incorrect. Then, the absorption in the wind outside the cylinder defined by the orbit was underestimated by ∼40 orders of magnitude. Furthermore, they assumed a uniform and rather low wind temperature, of 5000 K. In reality, the wind is Compton-heated on the side of the X-ray source to temperatures about two orders of magnitude higher (strongly reducing the free-free opacity with respect to the treatment of BFP02). Also, the jet model of BFP02 was relatively simplified, assuming that emission at a given frequency is emitted entirely at a single point along a linear jet, and it did not explain the phase lags.

Table 1. The average hard-state modulation depth and the phase shift [defined in equation (1) and calculated using the fitted model fluxes, see Fig. 1], from L06. The uncertainties are 1σ.

	2.25 GHz	8.3 GHz	15 GHz
M_ν	0.045 ± 0.027	0.138 ± 0.024	0.304 ± 0.018
$\phi_{\nu,\min}$	0.316 ± 0.096	0.179 ± 0.034	0.153 ± 0.022

In the present work, we consider models of the jet including its radial emission profile as well as its bending. We consider only the hard-state data. In modelling the stellar wind, we take into account its irradiation by the UV and X-ray photons, and propagation during the orbital motion of the primary. We model both the observed depth of the modulation as a function of frequency and the corresponding lags of the minima of the folded radio lightcurves with respect to the spectroscopic superior conjunction. This yields constraints on the jet velocity and emission profiles of the radio emission.

2 THE OBSERVED MODULATION

We first present the main observational results on the orbital variability of the radio emission from Cyg X-1, in order for this work to be self-contained. Fig. 1 shows the folded and averaged lightcurves from the Ryle and Green Bank radio telescopes in the hard state (L06). The 15 GHz lightcurve has the best statistical quality as well the highest modulation depth. As found in L06, its fitting requires three harmonics. On the other hand, it is sufficient to use a single sinusoidal dependence at 2.25 GHz and 8.3 GHz.

The fractional modulation depth is defined as in L06,

$$M_\nu \equiv \frac{F_\nu(\phi_{\nu,\max}) - F_\nu(\phi_{\nu,\min})}{F_\nu(\phi_{\nu,\max})}, \qquad (1)$$

where $F_\nu(\phi_{\nu,\max})$ and $F_\nu(\phi_{\nu,\min})$ are the maximum and minimum fluxes in the averaged and folded lightcurves, observed at the phases of $\phi_{\nu,\max}$ and $\phi_{\nu,\min}$, respectively, and the phase lags, given by $\phi_{\nu,\min}$. Here, $\phi = 0$ corresponds to the spectroscopic superior conjunction of the X-ray source, and ϕ is within the 0–1 interval. Table 1 gives the values of M_ν and $\phi_{\nu,\min}$ of L06. They constrain the parameters of the binary and the jet.

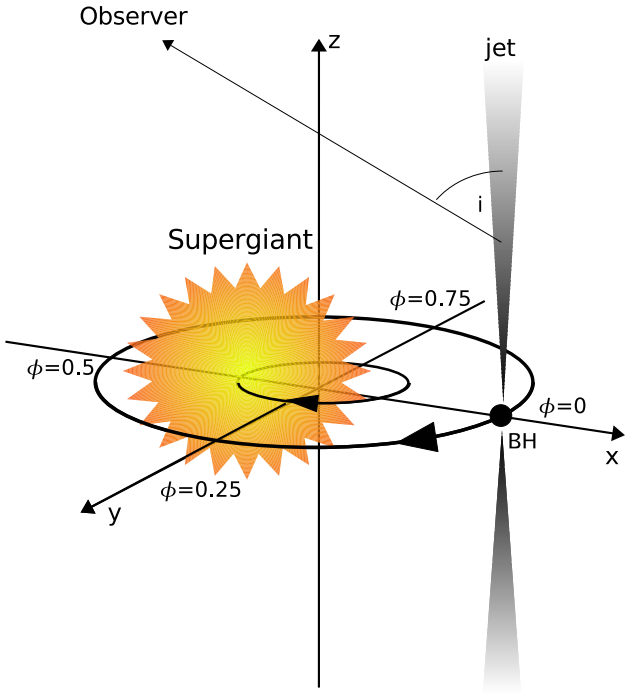

Figure 2. A schematic representation of Cygnus X-1 in the phase $\phi = 0$, with a fast jet. (Note that the counter-jet has not yet been observed.) The centre of mass is located within the primary. The observer is in the xz plane.

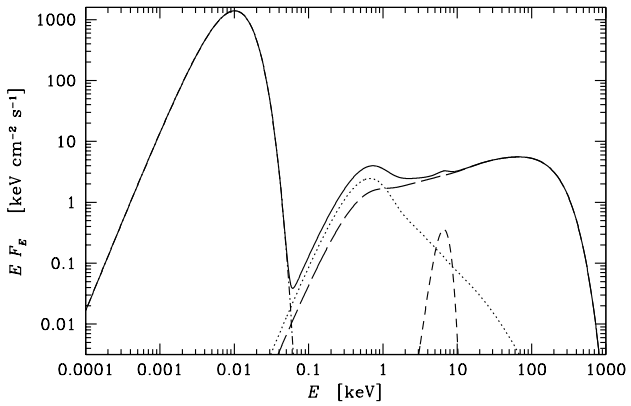

Figure 3. A characteristic intrinsic spectrum of Cyg X-1/HDE 226868 composed of the UV blackbody from the primary at $T = 3 \times 10^4$ K (the dot-dashed curve) and a hard state X-ray spectrum from the vicinity of the black hole. The X-ray spectrum is from Frontera et al. (2001). The dots, long dashes and short dashes correspond to the soft X-ray excess, the main hard X-ray Comptonization component, and the Fe Kα line, respectively.

3 THE MODEL

3.1 The binary

A schematic picture of the binary including the jet is shown in Fig. 2. The centre of our coordinate frame is in the centre of mass, and the orbit is in the xy plane. The observer is in the xz plane. We note that if the the jet is precessing (which may explain the observed superorbital modulation, see Section 5.2 below), the jet axis will be inclined with respect to the binary plane. In our modelling of the orbital modulation below, we neglect this effect since the precession amplitude is only poorly constrained (e.g., L06) and the superorbital modulation may in principle be alternatively explained by an intrinsic cycle of the supergiant wind.

The inclination, i, remains relatively uncertain. On the basis of analysis of absorption lines, Gies & Bolton (1986a) estimated $i = 33^\circ \pm 5^\circ$. On the other hand, the polarimetric measurements of Dolan & Tapia (1989) yield 25°–67°. In our study, we consider the inclination range of 30°–60°.

We assume the black hole and the primary masses of $20\mathrm{M}_\odot$ and $40\mathrm{M}_\odot$ (Ziółkowski 2005), respectively, and a circular orbit. The radius of the primary is taken as $r_\star = 1.58 \times 10^{12}$ cm (Gies et al. 2003). Then, the separation corresponds to $a = 2.28 r_\star = 3.60 \times 10^{12}$ cm, and the orbital velocity is 3.13×10^7 cm s^{-1} and 1.56×10^7 cm s^{-1} for the black hole and the primary, respectively. We hereafter use a as the unit, as it gives a measure of the asymmetry in the photon paths during the orbital motion. The distance is assumed to be $D = 2$ kpc (Ziółkowski 2005).

3.2 The wind

We assume the wind to be smooth, spherically symmetric and radiatively driven. We follow Schaerer (1996) and Santolaya-Rey, Puls & Herrero (1997) in assuming a simple wind stratification at its base. The inner part, which we do not consider here, is the stellar atmosphere. The outer part, i.e., the proper wind, is parametrized by the velocity law,

$$v(r) = v_\infty \left(1 - \frac{r_0}{r}\right)^\beta, \qquad r \geq r_\star, \tag{2}$$

where v_∞ is the terminal wind velocity,

$$r_0 = r_\star \left[1 - \left(\frac{v_\star}{v_\infty}\right)^{1/\beta}\right], \tag{3}$$

and the lower boundary of the wind at $r_\star$ is chosen to correspond to the isothermal sound speed,

$$v_\star \equiv v(r_\star) = \sqrt{\frac{kT_\star}{\mu m_\mathrm{H}}}, \tag{4}$$

where k is the Boltzmann constant, m_H is the hydrogen atom mass, μ is the mean molecular weight, and $T_\star$ is the temperature of the atmosphere, respectively. The particle number density at r is related to the mass-loss rate, $\dot{M}$, and and $v(r)$ via the continuity equation,

$$n(r) = \frac{-\dot{M}}{4\pi m_\mathrm{H} \mu r^2 v(r)}. \tag{5}$$

Note that equations (2–5) apply to a star at rest. Below, we apply those equations taking into account the orbital motion, with $r - r_\star$ measuring the distance travelled by a wind element (see below for details). We adopt $-\dot{M} = 2.6 \times 10^{-6} \mathrm{M}_\odot$ yr^{-1} (Gies et al. 2003), $v_\infty = 1.58 \times 10^8$ cm s^{-1}, $\beta = 1.05$ (Gies & Bolton 1986b), and $T_\star = T_\mathrm{eff}$ where T_eff is the effective temperature taken as 3×10^4 K (Ziółkowski 2005). This temperature at the assumed stellar radius yields $L_\star \simeq 1.5 \times 10^{39}$ erg s^{-1}. For calculating μ, we assume the wind to be ionized with the abundances for an O9.7 Iab star (Lamers & Leitherer 1993), which yields $\mu = 0.68$. We allow

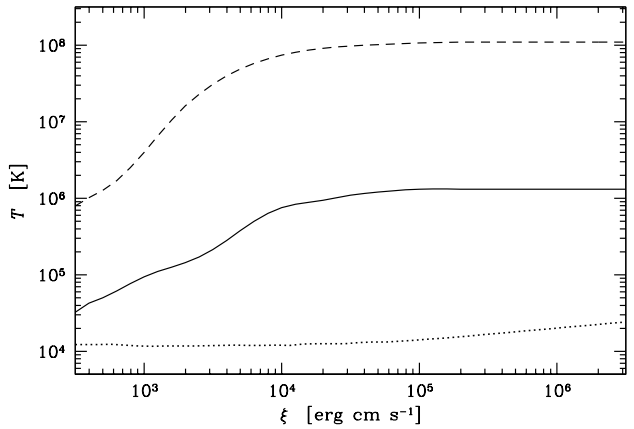

Figure 4. The gas temperature as a function of the ionization parameter calculated using XSTAR. We show the results for three irradiating spectra: the composite X-ray/UV spectrum of Fig. 3 (solid curve), the stellar 3×10^4 K blackbody (dotted curve), and the hard-state X-ray spectrum (dashed curve).

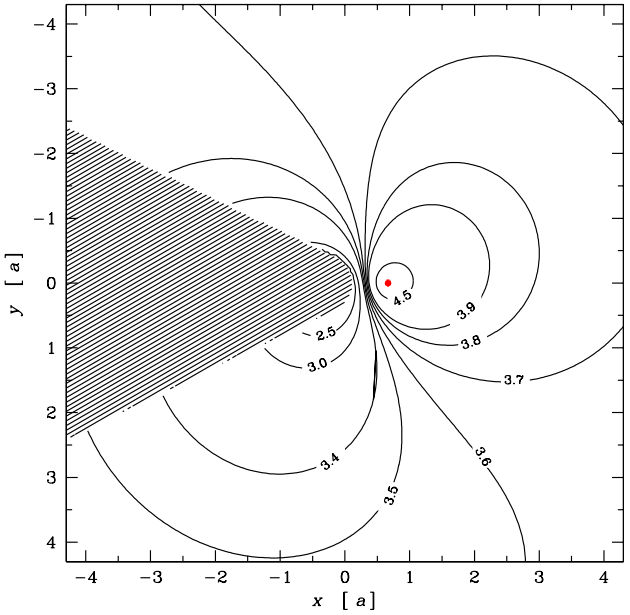

Figure 5. The distribution of $\log\xi$ in the plane of the orbit (the phase of $\phi=0$ corresponds to the observer on the left-hand side). The corresponding values of T are given by the solid curve in Fig. 4. The length unit is the separation, a. The hatched area covers the primary and the wind shadowed by it from the influence of the ionizing source. The small dot represents the position of the black hole. The slight asymmetry of the contours with respect to the line joining the star centres results from their (clockwise) orbital motion and the finite wind velocity.

the wind to extend out to the infinity, which assumption has a negligible effect on its absorption.

We note that, with the exception of a very dense wind region close to the stellar surface, the wind is optically thin for both X-ray and UV photons. The resulting optically-thin approximation allows us to greatly simplify calculations of the wind structure. In this approximation, the radiation field at a distance R away from a source of the luminosity, L, is determined only by the geometrical dilution, L/R^2, with no radiative transfer calculations being necessary. Moreover, at each point in the cloud with the number density, n, the state of the gas for a given spectral shape depends solely on the ionization parameter,

$$\xi \equiv \frac{L}{nR^2} \tag{6}$$

(Tarter, Tucker & Salpeter 1969). Thus, we can apply the results of a single model to a number of conditions with the same value of ξ. Based on the results of Kallman & McCray (1982), we apply the optically-thin approximation for $\xi > 10^{2.5}\,\mathrm{erg\,cm\,s^{-1}}$.

In order to calculate the ionization and temperature structure of the wind, we use the XSTAR photoionization code (Bautista & Kallman 2001). It calculates the state of the gas surrounding an ionizing radiation source. The gas is assumed to have a constant density but using the optically thin scaling law allows us to apply the results to the optically-thin part of the wind.

The illuminating source is assumed to have the spectrum equal to the sum of the hard-state spectrum of Cyg X-1 as modelled by Frontera et al. (2001) and the primary blackbody spectrum of $T_\star = 3\times10^4$ K, shown in Fig. 3. Our model spectrum is relatively similar to that of the model #5 of Kallman & McCray (1982). We stress that in spite of the primary having the luminosity about two orders of magnitude higher than that of the X-ray source, it is necessary to include both sources in the calculations. In particular, the gas temperature reaches the Compton temperature, T_C, in the limit of full ionization,

$$T_\mathrm{C} = \frac{\int EF_E\mathrm{d}E}{4k\int F_E\mathrm{d}E} \tag{7}$$

(e.g., Begelman, McKee & Shields 1983), corresponding to the balance of the Compton gains and losses only. Although the denominator is almost completely dominated by the blackbody emission, the dominant contribution to the numerator is from near the high-energy cutoff of the X-ray spectrum (in general, it is the case for any spectrum harder than $F_E \propto E^{-2}$). The Compton temperature of the X-ray component alone is as high as $\sim10^8$ K (see Fig. 4). Then, the addition of the stellar blackbody increases the Compton cooling [the denominator of equation (7)] and reduces T_C approximately by the ratio between the two luminosities, i.e., by two orders of magnitude, to $\sim10^6$ K.

The stellar blackbody emission has $L_\star \simeq 1.5\times10^{39}$ erg s^{-1}, whereas the X-ray luminosity is only $L_\mathrm{X} \simeq 2\times10^{37}$ erg s^{-1} (see also the data compilation in Zdziarski et al. 2002). We note that when calculating the ionization parameter, ξ [equation (6)], XSTAR uses only the luminosity in the 13.6 eV–13.6 keV range, equal to 3.2×10^{38} erg s^{-1} in our case. However, the full spectrum is used in calculations of the temperature structure and the distribution of different ions. The dependencies of $T(\xi)$ for the entire spectrum of Fig. 3 and its two components separately are shown in Fig. 4.

We assume that the entire radiation source is located at the position of the black hole (and thus R is the distance from the black-hole center). This approximation allows us to use XSTAR with a single input spectrum of Fig. 3 and for a range of the gas density. Although it introduces relatively large errors close to the binary plane, it reproduces

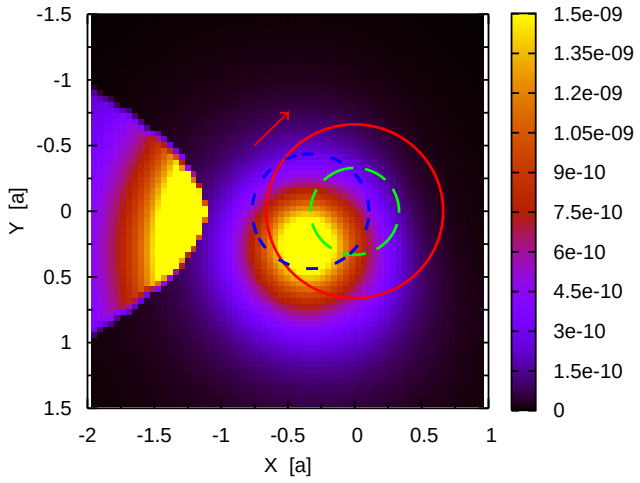

Figure 6. A map of the free-free absorption coefficient at 15 GHz at the height of $2r_\star$ above the orbital plane. The phase of $\phi = 0$ corresponds to the observer on the left-hand side. The image of the primary lags by 43° with respect to its actual position, shown by the short-dash circle, due to the stellar motion and the finite wind velocity. The solid and long-dash circles give the orbits of the black hole and the primary, respectively. The arrow shows the direction of the orbital motion. The wind shadowed from the X-ray irradiation by the primary is seen on the left.

well the actual temperature of the gas away from the plane, which region is important for calculating absorption of the jet emission.

Note that the gas density in the the inertial frame changes with the binary motion. In this frame, the wind density at a given point has to be calculated taking into account both the past motion of the primary and the motion of the wind. However, we neglect the effects of the orbital motion and rotation on the initial wind velocity. We also neglect the dynamics of the wind, e.g., effects of gravity and radiation.

We then calculate the wind ionization structure, and the resulting temperature distribution. The distribution of $\log \xi$ in the orbital plane is shown in Fig. 5. Because of a high density close to the surface of the primary, the optically-thin approximation breaks down there. However, this region does not contribute to absorption of the radio emission, which originates at relatively large distances from the primary. Though the region shadowed by the primary does not contribute to that absorption, we also calculate its temperature, based the dotted curve in Fig. 4. In the vicinity of the black hole, $\log \xi \gtrsim 4.5$, the wind is completely ionized and its temperature equals $T_{\rm C}$. Note that since the wind reaches its terminal velocity far away from the orbital plane, $n(r) \simeq n(R) \propto R^{-2}$. There, ξ reaches a constant, $\log \xi \simeq 3.6$ in our case, which corresponds to $T \simeq 3.2 \times 10^5$ K.

The free-free absorption coefficient (in cgs units) is (Rybicki & Lightman 1979),

$$\alpha_\nu = 0.018 T^{-3/2} Z^2 n_{\rm e} n_{\rm i} \nu^{-2} \bar{g}_{\rm ff} \ {\rm cm}^{-1}, \quad (8)$$

where $n_{\rm e}$ and $n_{\rm i}$ is the number density of electrons and ions, respectively. The velocity averaged Gaunt factor, $\bar{g}_{\rm ff}$, is approximated as

$$\bar{g}_{\rm ff} = 9.77 + 1.27 \log \frac{T^{3/2}}{Z\nu} \quad (9)$$

(Leitherer et al. 1995). For simplicity, we hereafter use $Z = 1$. Combining equations (2–3), (5) and (8–9), and using the numerical values assumed above, we obtain,

$$\alpha_\nu(r) = \frac{4.38 \times 10^{67} \bar{g}_{\rm ff}}{T^{3/2} r^4 \nu^2} \left(1 - \frac{1.56 \times 10^{12}}{r}\right)^{-2.1} {\rm cm}^{-1}. \quad (10)$$

In equations (8-10), T is in K, r is in cm and ν in Hz. We integrate the absorption coefficient along the line of sight from the place of radio emission at each phase to the observer, which gives us the optical depth and, in turn, the observed flux, F_ν.

As a result of the stellar motion and the finite wind velocity, the image of the primary reflected in the wind density, or the absorption coefficient, is phase-lagged with respect to the actual position of the primary at that time. We illustrate this effect in Fig. 6. It shows the absorption coefficient at the height of $z = 2r_\star$ above the orbital plane. We see a shift of the stellar image with respect to the actual primary position. The effect is visible here because the velocity of the wind is larger than the orbital velocity by only one order of magnitude, with the wind travelling the distance of $\sim 17.5a$ away from the stellar surface during one orbital period. This phase lag of the primary increases with the height above the orbital plane, and will by itself cause a phase shift in the orbital modulation of the radio emission with respect to the actual ephemeris. We take it into account in our calculations; however, we find it cannot by itself explain the observed phase lags. We also see the shadow wind in Fig. 6. Because of its relatively low temperature, it has higher free-free optical depth than the rest of the wind.

3.3 The jet

We assume that the radio emission originates in the jet. We neglect its transverse size and consider only its longitudinal structure. We assume that the geometry of the jet is directly defined by the initial condition at its base, namely the initial vertical velocity, v_0, the acceleration, a_0, and the perpendicular instantaneous orbital velocity, $2\pi R_{\rm BH}/P$, where $R_{\rm BH}$ is the orbital radius of the black hole. (Here, we do not take into account a possible jet precession and thus v_0 and a_0 have only vertical components.) We assume a continuous jet moving away from the place of the ejection. The trajectory of a jet element has the parametric form,

$$x(t) = R_{\rm BH} \cos(2\pi\phi) - \frac{2\pi t}{P} R_{\rm BH} \sin(2\pi\phi), \quad (11)$$

$$y(t) = R_{\rm BH} \sin(2\pi\phi) + \frac{2\pi t}{P} R_{\rm BH} \cos(2\pi\phi), \quad (12)$$

$$z(t) = v_0 t + \frac{1}{2} a_0 t^2, \quad (13)$$

where t is the time elapsed from the ejection. If the jet is fast, it remains nearly perpendicular to the orbital plane, as shown schematically in Fig. 2. For a slower jet, the relative contribution from the orbital velocity is important, and it bends, i.e., its position at a given radius lags behind the black hole. The projection of the motion of a single blob in the jet onto the orbital plane forms a spiral. Fig. 7 shows two examples for $v_0 = 0$ and two different values of a_0.

We then consider the jet emissivity profile. The simplest one corresponds to discrete emission, where each point of the

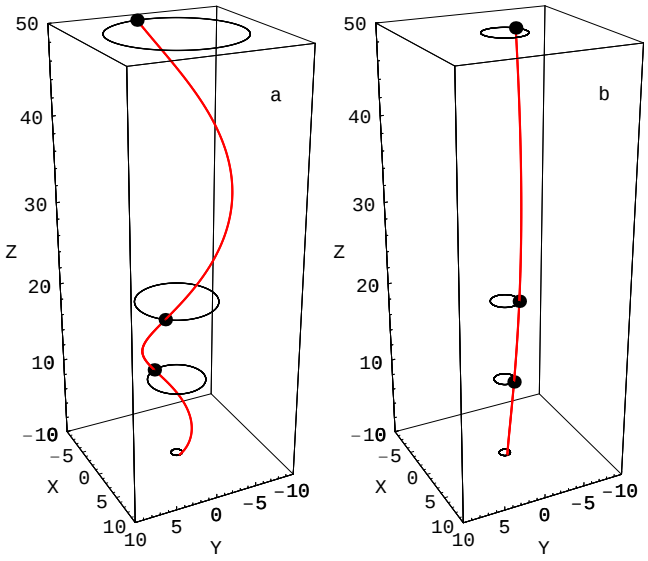

Figure 7. Two jets with $v_0 = 0$ and a low and a high acceleration, (a) 5×10^2 cm s^{-2}, (b) 5×10^3 cm s^{-2}, respectively. The black hole orbit is shown in the orbital plane, and three circles above it show the jet orbit at the height of $z = 10$, 20 and 50a.

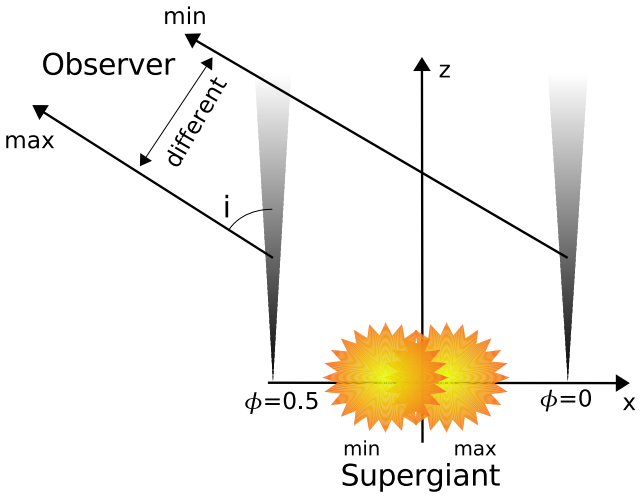

Figure 8. A schematic representation of the system, illustrating the difference between the lines of sight at $\phi = 0$ and 0.5. The optical paths at these two phases differ from each other both inside and outside the cylinder defined by the black hole orbit.

jet emits a (single) different frequency (which approximation was used by BFP02). As a more realistic parametrization of continuous jet emission, we use a double-power-law profile,

$$S_\nu(z') = \frac{K_\nu (z'/\mu_\nu)^{n_\nu}}{1 + (z'/\mu_\nu)^{m_\nu}}, \qquad (14)$$

where $S_\nu(z')$ is the radio flux emitted at z' and K_ν, μ_ν, n_ν (> 0) and m_ν ($> n_\nu$) are ν-dependent parameters. The variable z' gives the distance along the jet from its base. Hence, only in the case of the fast, straight, jet, $z' \approx z$.

If we consider only relative emission profiles, without specifying the absolute value of the emitted flux, we can set K_ν to the value normalizing the profile to unity at the maximum. The maximum flux is emitted at

$$z' = \mu_\nu \left(\frac{m_\nu}{n_\nu} - 1\right)^{-1/m_\nu}, \qquad (15)$$

and $S_\nu(z') \propto (z')^{n_\nu - m_\nu}$ and $\propto (z')^{n_\nu}$ far above and far below the maximum, respectively. The profile normalized to unity is given by

$$S_\nu(z') = \frac{m_\nu}{n_\nu} \left(\frac{m_\nu}{n_\nu} - 1\right)^{(n_\nu/m_\nu)-1} \frac{(z'/\mu_\nu)^{n_\nu}}{1 + (z'/\mu_\nu)^{m_\nu}}. \qquad (16)$$

4 RESULTS

Orbital modulation is produced when the source of the radio emission travels through the wind and thus it is observed through different optical depths, as illustrated in Fig. 8. The depth of the modulation, its phase shift and the average transmitted flux depend on the spatial profile of the radio emission, the jet velocity profile, and the inclination, which dependencies we investigate.

In general, as it is apparent from Fig. 8, the difference between the lines of sight is not confined to the space inside the cylinder defined by the black hole orbit. Because of a strong dependence of the absorption coefficient on the distance from the primary, $\alpha_\nu \propto r^{-4}$, a small difference in the line of sight can strongly affect the observed modulation. It is therefore not correct to neglect the differences in the absorption outside the orbital cylinder (as it was done in BFP02).

4.1 Discrete jet emission

We first consider a simple model with a fast jet, perpendicular to the orbital plane. We compare the observed emission from points along the jet at $\phi = 0$ and 0.5. We show the results in Fig. 9. We see that the strength of the modulation is close to unity near the base of the jet, and then decreases fast with the height. However, the intrinsic jet emission is very strongly attenuated in the regions where the jet modulation is close to unity. Excluding these region, the fast decrease of the modulation strength with the height implies that the spatial emissivity profile at a given frequency has to be narrow in order to yield a substantial modulation. These considerations point to the relative narrowness of the parameter space where strong radio modulation by wind absorption can be achieved, and may explain why Cyg X-1 is the only binary showing radio modulation due to that process.

We then stress the importance of properly accounting for the system geometry, see Fig. 10. We plot here three normalized lightcurves for models with three different system geometries. First (dots), the position of the primary is fixed at the centre with the black hole revolving around it on a circular orbit, and the absorption is confined to the cylinder defined by the black hole orbit, as assumed by BFP02. Second (dashes), we keep the former assumption but take into account the entire absorption. Third (the solid curve), we consider the actual case with the stars orbiting around the centre of mass. In all cases, we assume the emission from a single point of the straight jet. We see that the shape of the dotted curve disagrees with the observed lightcurve, in particular, there is no absorption at $\phi = 0.25$–0.75. Then,

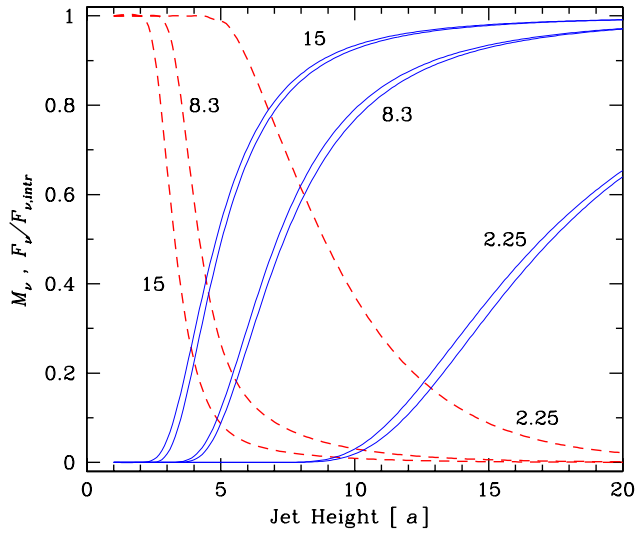

Figure 9. The modulation depth (dashed curves) and the fractional transmitted flux (solid curves) at a given point along a jet seen at $i = 40°$. The transmitted fluxes are shown for both $\phi = 0$ (lower curve in pair) and 0.5. Each curve is marked with the corresponding frequency in GHz. The curves take into account the binary motion.

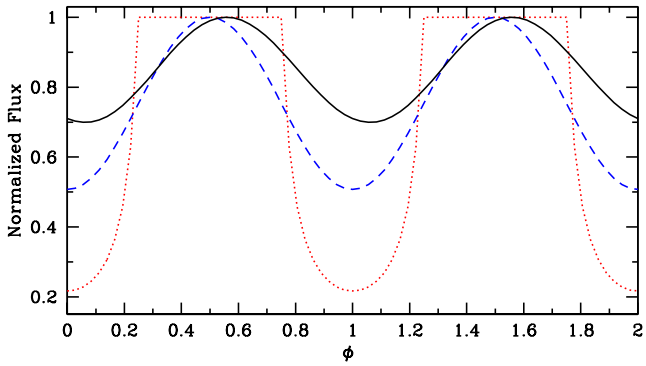

Figure 10. The normalized 15-GHz lightcurves for three different models. In all cases, we assume emission from a point of a straight jet at $z = 3.74a$ and $i = 40°$. The dotted curve assumes the fixed primary and the wind absorption model as in BFP02. The dashed curve is for the fixed companion but properly accounting for the absorption. The solid curve is for our model, with the stars orbiting around the centre of mass. The visible phase lag in this curve is due to the phase lag of the image of the primary (see Fig. 6), and it is $\simeq 0.06$ (corresponding to $\simeq 21°$).

accounting for the orbital motion of the both stars (solid curve) results in shallower modulation as compared to the case with the fixed companion. The phase shift of the minimum of the solid curve is due to the apparent displacement of the companion, see Section 3.2 and Fig. 6.

The difference between the minimum and maximum optical depth, and thus the modulation depth for emission from a single point, depends on the height above the orbital plane, z, and the inclination, i. We show this relationship in Fig. 11 for the observed modulation depths (Table 1). For example, $M_\nu \simeq 0.3$ at 15 GHz at $i = 40°$ corresponds to point emitting at $z \simeq 3.74a$.

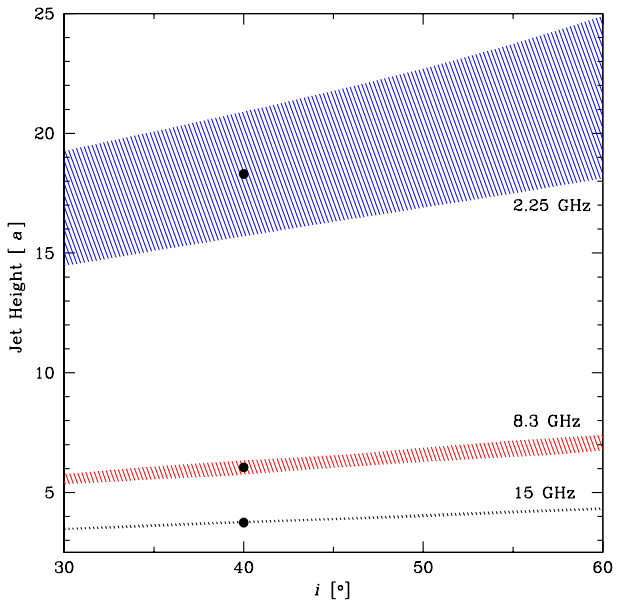

Figure 11. The shaded areas show the locations of the radio emission in the i–z space allowed by the observed modulation depths (Table 1), assuming discrete emission of a vertical jet. The black dots give the values assumed in Fig. 12 below.

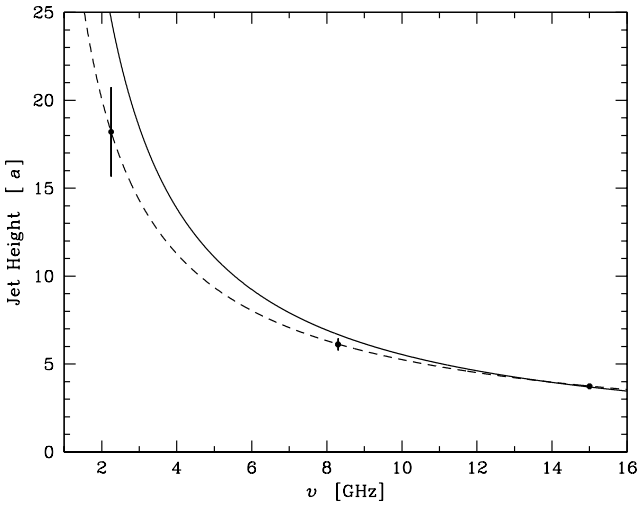

Figure 12. The three points shown in Fig. 11 with 1σ error bars, fitted with the $z \propto 1/\nu$ theoretical relationship (solid curve) and the best fit for $z \propto 1/\nu^\eta$ ($\eta = 5/6$; dashed curve).

The allowed emission regions at different frequencies are distinctly different, with lower frequencies emitted higher. For each ν, the region below the respective shaded area is occupied by points whose transmitted flux has higher modulation depth with respect to observed ones. Emission from points above the shaded area is modulated with lower amplitude.

We then compare our estimated emission distributions with the $z \propto 1/\nu$ relationship obtained by Blandford & Königl (1979). This relation follows from the position of the (photospheric) height where the jet becomes optically thin for synchrotron self-absorption. The three points shown in

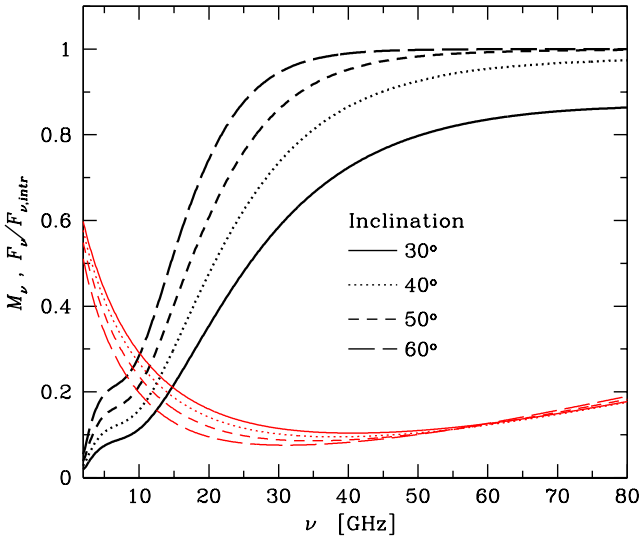

Figure 13. The relationships between M_ν and ν based on equation (18), for four values of i. The heavy and light curves correspond to the modulation depth and the fractional transmitted flux, respectively.

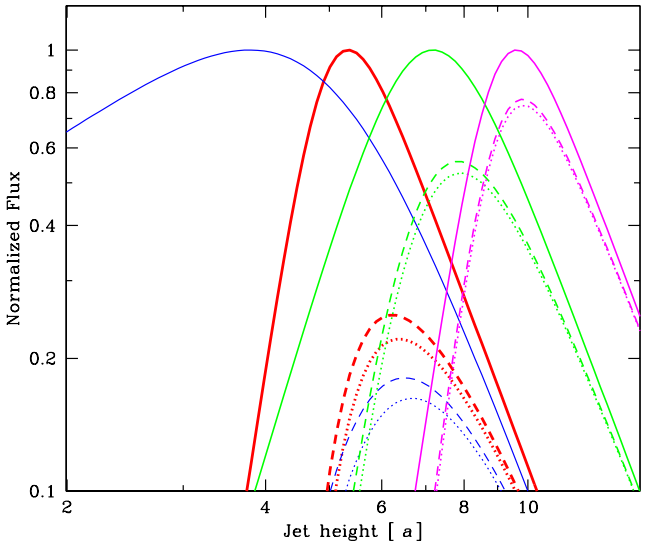

Figure 14. Examples of the intrinsic double-power-law profiles normalized to unity at the maximum (solid curves), together with the transmitted profiles for $\nu = 8.3$ GHz, $i = 40°$, and $\phi = 0.5$ (dashed curves) and $\phi = 0$ (dotted curves). The red, blue, green and magenta curves correspond to $(\mu_\nu/a,\, n_\nu,\, m_\nu)$ equal to $(5, 10, 14)$, $(5, 1, 5)$, $(7, 5, 9)$, $(9, 10, 14)$, respectively.

Fig. 11 have been fitted (including the errors on z estimated from Fig. 11) with $z = A/\nu$, where $A \propto L_{\rm J}^{2/3}$, and $L_{\rm J}$ is the jet power in relativistic electrons and magnetic fields (Blandford & Königl 1979). The best-fit relation,

$$\frac{z}{a} = \frac{55.4\,{\rm GHz}}{\nu}, \qquad (17)$$

shown in Fig. 12, does not agree with our model (based on the observed modulation depths) for 2.25 and 8.3 GHz within the 1σ error ranges. However, it does agree with the data within their 90 per cent confidence intervals. We also plot the best-fit curve for a general power law dependence, for which we find,

$$\frac{z}{a} = \frac{A}{(\nu/1\,{\rm GHz})^\eta}, \quad \eta \simeq 5/6, \quad A \simeq 35.8. \qquad (18)$$

Thus, the best-fit power-law index is only slightly lower than that given by Blandford & Königl (1979). The relationships at other inclinations than 40° are slightly different, but generally the heights of the 2.25 GHz and 8.3 GHz emission is slightly less than that predicted by equation (17).

We then obtained the positions and modulation depths for other frequencies extrapolating the observed modulation depths using equation (18), see Fig. 13. The curvature of the modulation depth at the low-frequency end results from changes of the apparent orbital separation related to the displacement of the primary image due to the motion of both stars and the finite wind velocity (see Fig. 6). At $\nu \gtrsim 40$ GHz, $M_\nu \to 1$, i.e., the emission at the minimum is then very strongly absorbed. The phase-averaged fractional transmitted flux above 40 GHz is $\sim$0.1. We also see that an increase of i increases the modulation depth.

4.2 Double-power-law profile

As an approximation to realistic jet emission, we consider double-power-law profiles, equation (14). This form of the spatial distribution can closely reproduce detailed jet models, e.g., those of Hjellming & Johnston (1988) and Kaiser (2006). In Fig. 14 we show examples of that profile for a number of parameters together with the same profiles transmitted through the wind at the phases of $\phi = 0$ and 0.5. The difference between the transmitted fluxes integrated over the jet length at those two phases gives (approximately, as the true minima have some phase shifts) the modulation depth. We can see that the higher the point of emission along the jet, the lower the difference between the two transmitted profiles, and hence the lower modulation. The low-z ($\propto z^{n_\nu}$) branch of the profiles is almost completely absorbed and thus the shape of the transmitted profiles and the modulation depth is only weakly dependent on n_ν. However, the fractional transmitted flux (i.e, with respect to the unobserved intrinsic emission) does significantly depend on n_ν.

We have then created contour maps in the location–width plane. The former is represented by μ_ν, determining the profile peak [equation (15)], and the latter, by $m_\nu - n_\nu$, which is approximately [see equation (16)], inversely proportional to its width. Fig. 15 shows two maps corresponding to profiles with significant ($n_\nu = 1$) and small ($n_\nu = 10$) contributions to the intrinsic emission from below the profile maximum. The hatched areas represent the profiles with the observed modulation depth (Table 1) at different ν and i. As it can be inferred from Fig. 15, broader profiles correspond to lower z and higher i. Also profiles emitted at lower z have lower fractional transmitted fluxes. On the other hand, narrow profiles have to be emitted at higher z, and have the value of μ_ν approximately equal to the corresponding location of point emission profiles shown in Fig. 11.

The areas of the parameter space allowed by the observations are smaller for $n_\nu = 10$ because these profiles are narrower, and the corresponding modulation depth quickly decreases with the increasing height of the jet. These pro-

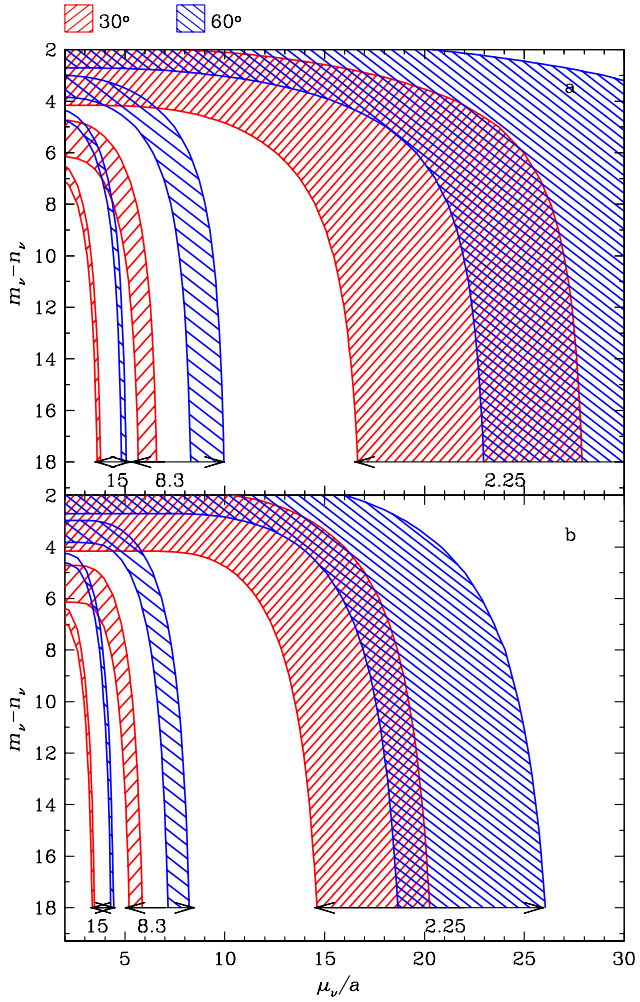

Figure 15. The regions in the space of the peak position, μ_ν, vs. $m_\nu - n_\nu$ of the double-power-law emissivity profile allowed by the observed modulation depths (Table 1), for different values of ν and i and for (a) $n_\nu = 1$ and (b) $n_\nu = 10$.

files are also shifted towards lower values of μ_ν than the $n_\nu = 1$ profiles. These effects are more prominent at lower frequencies.

The phase shifts we are able to obtain for the double-power-law profile along a straight jet are within about ± 0.08 (due to the effects of the finite wind velocity coupled with the orbital motion). They are not sufficient to explain the observed phase lags (Table 1).

4.3 A slow jet

Here, we consider the jet bending due to its initial (binary) motion together with the black hole, see Section 3.3. As it can be seen from Fig. 7, a curved jet bends outside the cylinder defined by the black hole motion. Thus, the amplitude of the optical depth variations is higher than in the case of the vertical jet, which will then increase the strength of the modulation. Also, the resulting lag behind the compact object will lead to a lag in the phase of the maximum absorption (i.e., the minimum flux), as observed.

In general, the flux phase profile depends on the inclination, i, the profile parameters (μ_ν, m_ν, n_ν), and on the velocity profile, given by v_0 and a_0. Then, in order to reduce the parameter space, we consider here only two velocity profiles, one with $v_0 > 0$ and $a_0 = 0$ (corresponding to acceleration only at the jet base), and one with $v_0 = 0$ and a constant $a_0 > 0$. In addition to the constraints from M_ν, we now also take into account the constraints from the phase lag of the minimum flux, $\phi_{\nu,\rm min}$ (Table 1).

First, we find that *no* jet with $v_0 > 0$ and $a_0 = 0$ can satisfy the observational constraints. At most, the observational constraints can be satisfied at only one of the observed frequencies. Then, we consider the case with $v_0 = 0$ and constant $a_0 > 0$, which we find can easily satisfy those constraints. Fig. 16 shows the ranges of the parameters allowed by the data for a selection of values of a_0. We show the results for $n_\nu = 1$ and 10, analogous to Fig. 15 for the case of the straight jet. The coloured regions are those where both of the constraints are satisfied for a given frequency. Such regions exist for each of the observed frequencies and given an appropriate choice of a_0 [cm s^{-2}] in the range of $(1.1\text{–}1.4) \times 10^3$ for $i = 30°$, $(1.1\text{–}1.5) \times 10^3$ for $i = 40°$, $(1.2\text{–}1.6) \times 10^3$ for $i = 50°$ and $(1.2\text{–}1.7) \times 10^3$ for $i = 60°$. The values of a_0 used in Fig. 16 correspond approximately to the middle of these ranges. It is, of course, possible that the jet acceleration is not constant, but as this is not required by the data, we do not consider such models. We also show the corresponding fractional transmitted fluxes. They are allowed to be rather large, typically $\sim$0.2–0.5 for broad profiles ($n_\nu = 1$) and $\gtrsim$0.5 for narrow profiles ($n_\nu = 10$).

The acceleration is relatively slow and the jet will be curved, with the curvature somewhere in between those shown in Fig. 7(a) and (b). At the distance of $20a$ (7.2×10^{13} cm), around which the 2.25 GHz radiation is emitted in our model, a jet with $a_0 = 1.3 \times 10^3$ cm s^{-2} will reach $v \simeq 4.3 \times 10^8$ cm s^{-1} during 3.3×10^5 s. At this point, it will lag behind the black hole by $\sim 170°$ and it will be at the distance from the orbital axis of 4.5 times the radius of the black-hole orbit.

5 DISCUSSION

5.1 General features of the model

There are a few essential features of our model, necessary to account for the observed orbital modulation depths and the phase lags. One is the wind heating due to the irradiation by the X-rays. This naturally creates a strong temperature anisotropy, and consequently strong anisotropy of the free-free absorption coefficient. Though the X-ray luminosity is $\sim 10^2$ times lower than the UV luminosity of the primary, Compton heating is proportional to the *product* of the irradiating energy flux and the photon energy. The latter is $\sim 10^4$ times higher for the X-rays than for the UV, and consequently, the X-ray heating is $\sim 10^2$ times higher than the UV heating. We also point out that the range of the temperatures of the wind obtained by us, $T \simeq 10^{4.5}$–10^6 K, is in full agreement with that found from *Chandra* soft X-ray observations of Cyg X-1 by Miller et al. (2005).

For test purposes, we have also run models with a uniform wind temperature equal 10^4 K. They required strong fine-tuning in order to achieve the observed modulation

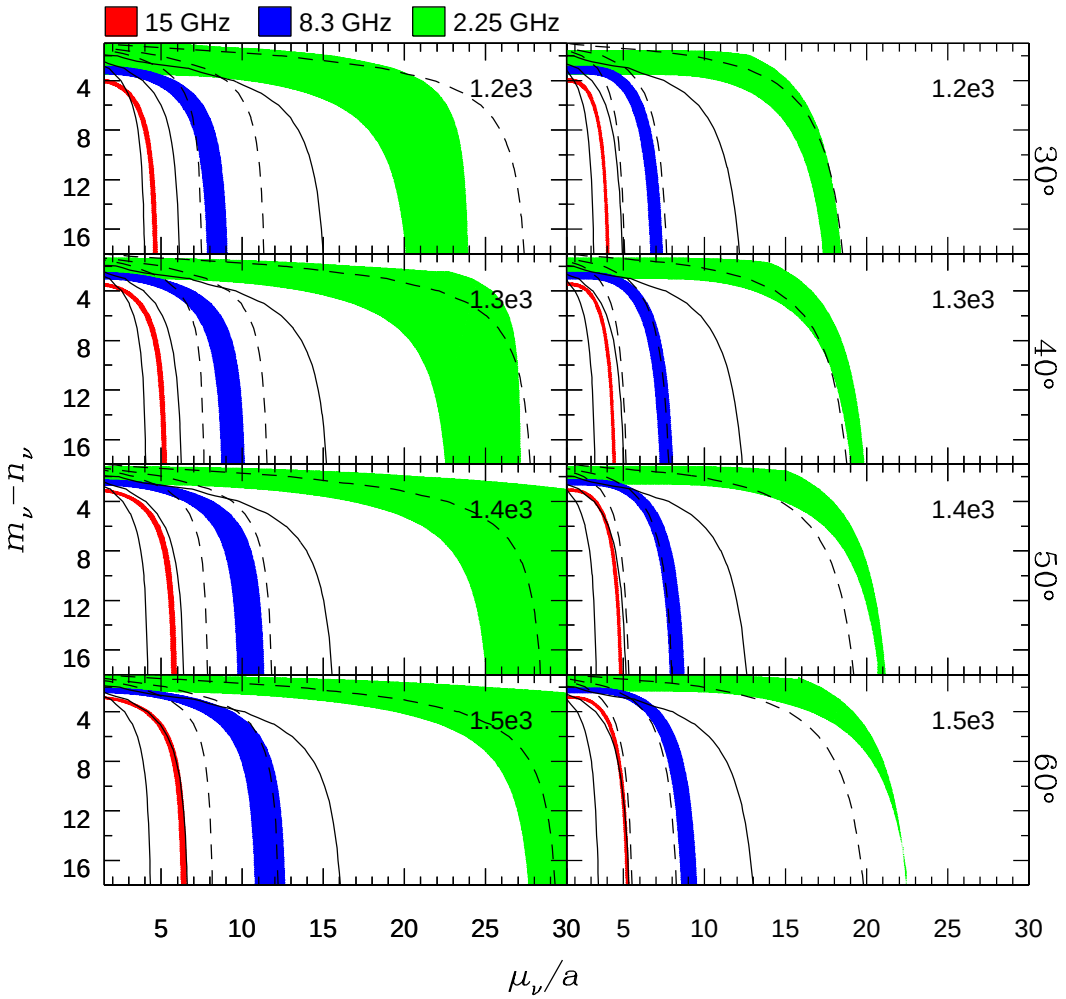

Figure 16. Constraints on the double power-law emissivity profiles, with μ_ν giving the position of the peak emission, and $m_\nu - n_\nu$ its width, for a jet with $v_0 = 0$ and constant acceleration (given on each panel in units of cm s^{-2}). The left and right columns correspond to $n_\nu = 1$ and 10, respectively, and each row correspond to a different value of i (marked on the right). The parameters allowed by both the observed modulation depth and the phase lag are marked by the coloured areas separately for each ν. The solid and dashed curves correspond to the fractional transmitted fluxes of 0.1 and 0.5, respectively, at $\nu = 15$ GHz, 8.3 GHz and 2.25 GHz, from left to right.

depths, as well as very low resulting transmitted fraction of the intrinsic jet flux, $\lesssim 10^{-2}$. Inclusion of X-ray heating resolves those problems.

Another essential feature is the required low velocity of the bulk of the mass of the jet, necessary for the jet bending required to account for the observed phase lags of the flux minima (with respect to the superior conjunction of the black hole). The velocity is nonrelativistic within the jet region constrained by the data. The jet bending results then from the initial jet velocity in the binary plane (due to the orbital motion of the black hole) being comparable to its vertical velocity component. We have searched for other ways to account for the observed phase lags, and have found none. In particular, the lags associated with the finite wind velocity together with the motion of the primary star cannot account for the observations.

We note that the modulation depth increases with ν in the 2.25–15 GHz range. Our model reproduces this increase. Not unexpectedly, it predicts the depth of the orbital modulation to increase further at $\nu > 15$ GHz. It would be of high interest to test this prediction observationally. We note that there have been rather few observations at $\nu > 15$ GHz so far (Fender et al. 2000; note some errors in the observation dates given there), insufficient for that test.

A related issue is the shape of the *intrinsic* jet spectrum. The observed average, absorbed, spectrum, is approximately given by $F_\nu \propto \nu^\alpha$ with $\alpha \simeq 0$ in the $\sim$2–200 GHz range (Fender et al. 2000). The intrinsic spectrum of the jet is also likely to be a power law, in general with a value of α allowed to be different than 0. However, if the intrinsic index is substantially different from 0, then obtaining the $\alpha \simeq 0$ power law would require a specific power-law absorption law. We can obtain it with our model. However, given the relatively large number of the free parameters compared to the relatively few observational constraints, the resulting model constraints would be rather loose. On the other hand, the most natural way to obtain the observed $\alpha \simeq 0$ is with the transmission fraction through the wind being high, close to 1. As we show in Fig. 16, there is a relatively large pa-

rameter space with that fraction being high, $\gtrsim 0.3$, and thus this is indeed possible.

The radio maps obtained from observations at 8.4 GHz (S01) show the jet to form an extended feature. The flux reaches the maximum at the core of an angular size of $\simeq 3$ mas, and then it decreases over ~ 12 mas away from it. For i from 60° to 30°, 3 and 15 mas correspond to (29–50)$a \simeq (1.0–1.8) \times 10^{14}$ cm and (140–250)$a \simeq (5–9) \times 10^{14}$ cm, respectively. Our constraints are for the distances along the jet of $z \lesssim 30a$ at 2.25 GHz and $z \lesssim 15a$ at 8.3 GHz. Thus, they apply only to the core of the jet.

Still, we can compare the predictions of our model with the radio maps of S01 at larger distances using the double-power-law profiles. We find that the observed extended structure of the jet is substantially more luminous than the predictions of our simple models. The propagation of the jet beyond the core may be affected by various effects, e.g., its moving away from the stellar wind region, and this issue is beyond the scope of the present work.

We note that the 2.25–15 GHz monitoring data used by us are integrated over the entire observed source. The emission at a given frequency from outside of the jet core is very unlikely to be modulated by the stellar wind. Thus, the fractional modulation of the emission close to the jet base has to be actually somewhat higher than that used by us, in order to account for the constant part emitted outside the core. According to the results of S01, the 8.4 GHz flux from the extended part is less than or similar to that of the core. Then, the fractional modulation of the core emission should be higher by a factor $\lesssim 2$ than that averaged over the entire structure, but the values of the phase lags are not affected.

It is possible to reproduce the core emission profiles with such a modulation depth in our model. The required profiles are located to the left of the 8.3 GHz region in Fig. 16, which introduces only a small change in the value of the acceleration, reducing it only by at most 10 per cent. Then, the results of S01 show that the 15.4 GHz emission is mostly in the core of the extend of $\lesssim 2$ mas, with only $\lesssim 10$ per cent of the emission outside the core. This is approximately compatible with our spatial emission profiles. Then, no radio maps are available at ~ 2 GHz.

Our models yield the jet acceleration of $\sim (1.1–1.7) \times 10^3$ cm s^{-2}. At $20a$, the jet achieves the velocity of $\sim (4–5) \times 10^8$ cm s^{-1}, and ~ 3 times that at $200a$, i.e., $\ll c$ in both cases. On the other hand, S01 has estimated the jet velocity to be mildly relativistic based on the lack of the observed counter jet being explained by the relativistic Doppler beaming. The results of S01 combined with the constraints of Gleissner et al. (2004) (based on the lack of radio–X-ray correlations on m–h time scales) yield the jet velocity of $\simeq (0.5–0.7)c$. This requires an acceleration $\gtrsim 10^2$ times higher than that estimated by us. We note, however, that our results do not constrain at all the jet region at $z \gtrsim 30a$. Thus, the acceleration there can be much higher, e.g., due to the stellar wind density being much lower than in the inner jet region.

5.2 Superorbital modulation

Another argument for the relativistic bulk velocity of the jet electrons emitting synchrotron radiation is the presence of the superorbital (i.e., on a time scale much longer than the orbital period) modulation. The modulation, with the period of $\simeq 150$ d, is present in both radio and X-rays (e.g., Brocksopp et al. 1999a; L06). The standard (though not proven) explanation of that effect in Cyg X-1 (and a number of other X-ray binaries) is precession (e.g., Larwood 1998; L06). Then, the jet precession can cause the flux variability at this period if the jet is at least mildly relativistic. The radio data on the superorbital modulation are compatible with this picture as the modulation depth at the three monitored frequencies, 2.25, 8.3 and 15 GHz, is compatible with being constant, and there are no significant phase lags. We note, however, that those data do not require the jet velocity to be relativistic in the core, as the superorbital modulation can be caused by electrons outside it. Also, the required velocity can be as low as $\sim 0.1c$ if the (unknown) precession amplitude is $\sim 30°$.

On the other hand, we can provide here an explanation for the superorbital radio modulation without invoking a relativistic jet velocity. Namely, a precessing jet moves with respect to the wind structure (which is defined only by the binary orbit and does not precess). The line of sight from a given point in the jet, and thus the amount of the orbit-averaged free-free absorption in the wind, will then change with the superorbital phase (without phase lags). However, the modulation depth is frequency-dependent in this model. In principle, it is possible to find parameters of the system yielding the same modulation depth from 2 to 15 GHz, but it requires certain fine-tuning.

5.3 Two-flow jet

As we have discussed above, the observed phase lags of the orbital radio modulation require that the bulk of the jet mass is nonrelativistic within the region where most of the radio emission takes place. On the other hand, the non-detection of the counter jet and the superorbital radio modulation point to (though not completely require) relativistic bulk motion of most of the synchrotron-emitting electrons. This apparent contradiction may be reconciled provided that the jet contains two flows at different velocities, e.g., an outer slow part and a fast inner part.

Such a model for radio-emitting X-ray binaries has been recently proposed by Ferreira et al. (2006). It is based on an analogous, two-flow, model for extragalactic radio jets of Sol, Pelletier & Asséo (1989). The main contribution to the total jet power is an electron-proton plasma that is either nonrelativistic in X-ray binaries or mildly relativistic in AGN jets. This plasma is generated by an MHD process in a large-scale magnetic field anchored in the accretion disc. The second flow is composed of relativistic $e^{\pm}$ pairs, and it carries only a small fraction of the total power. It is produced in the inner regions of the MHD flow, where the pairs are created and then accelerated. The outer flow confines the inner one. In the AGN case, the outer slow flow is identified with kpc-scale jets, fuelling the radio lobes and hotspots, and the fast inner flow is identified with pc-scale jets and the superluminal motion (Sol et al. 1989). We note that the specific model of Ferreira et al. (2006) postulates that the threshold for pair production, forming the inner fast jet, is reached only above the accretion rates corresponding to the hard spectral state.

A massive disk outflow (linked with the super-Eddington mass transfer rate) has been proposed to exist

in the X-ray binary SS 433 (Zitter, Calvani & D'Odoricio 1991; Fabrika 1993, 2004). The outflow, with the velocity of $\sim 1.5 \times 10^8$ cm s^{-1}, is radiatively driven from outer parts of the accretion disc. Its direction is determined by the tilt of the disc and is subject to both precessional and nutational motions of the outer disc. Begelman, King & Pringle (2006) then postulated that the outflow is massive enough to deflect the relativistic jet launched from the vicinity of the accreting object and to align it with the outflow axis.

In the case of Cyg X-1, we may identify the slow flow with the one needed to explain the radio phase lags, and the fast one, with that at a relativistic motion explaining the invisibility of the counter jet and the superorbital modulation. However, this identification requires modifications of the above models to allow for the existence of the two flows already at lower accretion rates, corresponding to the hard spectral state.

We further note that our postulated slow (and dark) flow is very likely to be identical to that found by Gallo et al. (2005) to be required to power the radio lobes of Cyg X-1. The kinetic power of that flow was found by Gallo et al. (2005) to be comparable to the X-ray luminosity. On the other hand, Heinz (2006) found that the kinetic power carried by fields and radio-emitting electrons in the visible jet of Cyg X-1 was much smaller. This is in agreement with the picture in which the visible (fast) flow is confined by the dark (slow) one. Also, Heinz (2006) estimated the velocity of the dark flow powering the radio lobes of Cyg X-1 as $\gtrsim 6 \times 10^8$ cm s^{-1}. This is in agreement with the velocity constrained by the radio modulation, see Section 5.1 above.

5.4 Cyg X-3

Cyg X-3 is an example of another high-mass X-ray binary with the companion emitting strong wind and with very strong orbital modulation of X-rays, thought to be caused by absorption and scattering in the wind. It also has strong radio emission, most likely originating from a jet of that system. Still, no orbital modulation of the radio emission is seen (Hjalmarsdotter et al. 2004).

To explain this lack of modulation, we first point out that Cyg X-3 is a much more compact system than Cyg X-1. The orbital period of the former is only 4.8 hr. Cherepashchuk & Moffat (1994) have estimated its orbital separation as $a \simeq (2.2\text{–}3.9) \times 10^{11}$ cm, an order of magnitude less than that of Cyg X-1. The degree of asymmetry of the wind at a given height, z, is proportional to a/z. Thus, if the jet of Cyg X-3 emits a given radio frequency at the same height as Cyg X-1, its orbital modulation will be still much lower.

Furthermore, the companion star in Cyg X-3 is a Wolf-Rayet star, which mass loss rate, estimated as $-\dot{M} \simeq (3.6\text{–}29) \times 10^{-5} \mathrm{M}_\odot$ yr^{-1} (Ogley, Bell Burnell & Fender 2001), is much higher than that of the OB star in Cyg X-1. Thus, the radio emission originating relatively close to the jet base is likely to be completely free-free absorbed in Cyg X-3. The high mass-loss rate coupled with the small separation also makes the wind optically thick to X-rays, not allowing us to use our optically-thin model (Section 3.2).

The height from which a radio frequency is predominantly observed is then roughly at $z \propto L_{\rm J}^{2/3}$ (Blandford & Königl 1979). The power of the jet is, in turn, $L_{\rm J} \propto L_{\rm X}^p$, with $p \simeq 0.5$–1 (e.g., Migliari & Fender 2006). The X-ray luminosity of Cyg X-3 is $\sim$(10–100) times that of Cyg X-1 (e.g., Gallo, Fender & Pooley 2003; Vilhu et al. 2003). This consideration also points out to the height of radio emission in Cyg X-3 being significantly higher than that in Cyg X-1. Consequently, the wind at the radio-emitting region in Cyg X-3 is likely to be almost completely axially symmetric, resulting in no orbital modulation in the radio range.

6 CONCLUSIONS

Our main conclusions are as follows. We find the observational data on the orbital modulation of the radio emission from Cyg X-1 fully consistent with the emission originating in a jet. As postulated before, the modulation is caused by free-free absorption in the wind from the companion, with the line of sight changing during the orbital motion.

We find a crucial role of X-ray irradiation of the wind in enhancing its axial asymmetry with respect to the jet axis. The irradiation strongly increases the wind temperature, up to the Compton temperature of $\sim 10^6$ K, in the vicinity of the X-ray source, which then strongly reduces the free-free absorption on the side of the black hole. It also increases the overall wind temperature to $\gtrsim 3 \times 10^5$ K (except for the vicinity of the companion), which is about one order of magnitude above the star temperature. This reduces the constant component of the free-free absorption and allows the transmitted fraction of the radio emission to be close to unity. Consequently, the intrinsic jet emission is likely to be close to the observed flat radio spectrum (Fender et al. 2000). The wind temperatures calculated by us agree with those inferred from the *Chandra* data (Miller et al. 2005).

Another crucial requirement following from our study is the velocity of the bulk of the mass of the jet being nonrelativistic, $\sim 5 \times 10^8$ cm s^{-1}, in the jet core (within $\sim 10^{14}$ cm). It follows from the relatively large phase lags of the absorption maxima with respect to the spectroscopic zero phase. The only explanation of these lags appears to be a kinematic bending of the jet caused by the initial jet velocity in the binary plane (equal to the orbital velocity of the black hole) being comparable (though still substantially lower) to the jet vertical velocity in the region where most of the 2–15 GHz emission is produced. Also, the data imply that the above velocity is reached following an approximately constant acceleration within the core, while a rapid, instantaneous-like acceleration is ruled out.

However, the jet may then become mildly relativistic outside of the core, as implied by the lack of a detectable counter jet (S01). Also, the synchrotron-emitting electrons may have a relativistic bulk motion already in the core if the jet is composed of two components, a slow, heavy, dark outer flow, and a relativistic, light, and bright inner flow (as proposed by several authors in order to explain other observational features of jets).

We also consider the observed superorbital modulation of the radio emission, with the period of ~ 150 d. That modulation can be caused by the Doppler effect in a relativistic precessing jet. However, we find we can also explain that modulation by the free-free absorption varying due to the jet precession. When the precessing jet is inclined to-

wards the observer, the average absorption of its emission is weaker.

We construct specific models constraining the distribution of the radio emission at a given frequency along the jet. The lower the frequency, the higher up it is emitted, and thus it is less modulated by the absorption, as observed. Within the 90 per cent confidence intervals, our results are compatible with the $z \propto 1/\nu$ law of Blandford & Königl (1979). Our results are also compatible with the plausible values of the inclination of Cyg X-1, $\sim 30^\circ$–60°. For a given model, the higher the inclination, the deeper the modulation.

A prediction from our models is that the modulation depth should increase with frequency also at $\nu > 15$ GHz. Thus, future monitoring at those frequencies would be of great importance for our understanding of the jet structure.

We also consider the issue why there is no observed radio modulation in Cyg X-3, which system is also powered by wind accretion and which shows strong orbital modulation of its X-ray emission. We find a major reason for the lack of radio modulation is its orbital separation being an order of magnitude lower than in Cyg X-1, thus strongly reducing the wind asymmetry seen from the jet. Also, it has much higher both the wind rate and the luminosity, which both factors imply radio emission take place at higher heights than in Cyg X-1 (further reducing any asymmetry of the wind seen from the jet).

Finally, we point out that our treatment of the jet and the wind has still neglected their dynamical interactions. We also treat jet emission only in the core (where it is modulated), and do not model its observed extended component. These issues can be addressed in future work.

ACKNOWLEDGMENTS

We thank M. Sikora for valuable discussions, R. Goosmann, J. Poutanen and the referee for useful comments, C. Brocksopp for discussion of her results and the numerical code used in BFP02, and P. Lachowicz for providing us with the data shown in fig. 4 of L06. This research has been supported by the grants 1P03D01827, 1P03D01128 and 4T12E04727.

REFERENCES

Bautista M. A., Kallman T. R., 2001, ApJS, 134, 139
Blandford R. D., Königl A., 1979, ApJ, 232, 34
Begelman M. C., McKee C. F., Shields G. A., 1983, ApJ, 271, 70
Begelman M. C., King A. R., Pringle J. E., 2006, MNRAS, 370, 399
Bolton C. T., 1972, Nat, 235,
Bolton C. T., 1975, ApJ, 200, 269
Brocksopp C., Fender R. P., Larionov V., Lyuty V. M., Tarasov A. E., Pooley G. G., Paciesas W. S., Roche P., 1999a, MNRAS, 309, 1063
Brocksopp C., Tarasov A. E., Lyuty V. M., Roche P., 1999b, A&A, 343, 861
Brocksopp C., Fender R. P., Pooley G. G., 2002, MNRAS, 336, 699 (BFP02)
Cherepashchuk A. M., Moffat A. F. J., 1994, ApJ, 424, L53
Coe M. J., Bowring S. R., Court A. J., Hall C. J., Stephen J. B., 1983, MNRAS, 203, 791
Dolan J. F., Tapia S., 1989, ApJ, 344, 830
Fabrika S. N., 1993, MNRAS, 261, 241
Fabrika S., 2004, ASPRv, 12, 1
Fender R. P., Pooley G. G., Durouchoux P., Tilanus R. P. J., Brocksopp C., 2000, MNRAS, 312, 853
Fender R. P., Stirling A. M., Spencer R. E., Brown I., Pooley G. G., Muxlow T. W. B., Miller-Jones J. C. A., 2006, MNRAS, 369, 603
Ferreira J., Petrucci P.-O., Henri G., Saugé L., Pelletier G., 2006, A&A, 447, 813
Frontera F., et al., 2001, ApJ, 546, 1027
Gallo E., Fender R. P., Pooley G. G., 2003, MNRAS, 344, 60
Gallo E., Fender R., Kaiser C., Russel D., Morganti R., Oosterloo T., Heinz S., 2005, Nat, 436, 819
Gies D. R., Bolton C. T., 1982, ApJ, 260, 240
Gies D. R., Bolton C. T., 1986a, ApJ, 304, 371
Gies D. R., Bolton C. T., 1986b, ApJ, 304, 389
Gies D. R., et al., 2003, ApJ, 583, 424
Gleissner T., et al., 2004, A&A, 425, 1061
Han X., 1993, PhD thesis, New Mexico Inst. Mining and Technology
Haynes R. F., Lerche I., Murdin P., 1980, A&A, 87, 299
Heinz S., 2006, ApJ, 636, 316
Hjalmarsdotter L., Hakala P. J., Vilhu O., Hannikainen D. C., McCollough M., Pooley G. G., 2004, RevMexAA, 20, 216
Hjellming R. M., Johnston, K. J., 1988, ApJ, 328, 600
Kaiser C. R., 2006, MNRAS, 367, 1083
Kallman T. R., McCray R., 1982, ApJS, 50, 263
Lachowicz P., Zdziarski A. A., Schwarzenberg-Czerny A., Pooley G. G., Kitamoto S., 2006, MNRAS, 368, 1025 (L06)
Lamers H. J. G. L. M., Leitherer C., 1993, ApJ, 412, 771
Larwood J., 1998, MNRAS, 299, 32
Leitherer C., Chapman J. M., Koribalski B., 1995, ApJ, 450, 289
Marti J., Paredes J. M., 1995, A&A, 298, 151
Migliari S., Fender R. P., 2006, MNRAS, 366, 79
Miller J. M., Wojdowski P., Schulz N. S., Marshall H. L., Fabian A. C., Remillard R. A., Wijnands R., Lewin W. H. G., 2005, ApJ, 620, 398
Ogley R. N., Bell Burnell S. J., Fender R. P., 2001, MNRAS, 322, 177
Pooley G. G., Fender R. P., Brocksopp C., 1999, MNRAS, 302, L1
Priedhorsky W. C., Brandt S., Lund N., 1995, A&A, 300, 415
Rybicki G. B., Lightman A. P., 1979, Radiative Processes in Astrophysics, Wiley, New York
Santolaya-Rey A. E., Puls J., Herrero A., 1997, A&A, 323, 488
Schaerer D., 1996, A&A, 309, 129
Sol H., Pelletier G., Asséo E., 1989, MNRAS, 237, 411
Stirling A. M., Spencer R. E., de la Force C. J., Garrett M. A., Fender R. R., Ogley R. N., 2001, MNRAS, 327, 1273 (S01)
Tarter C. B., Tucker W. H., Salpeter E. E., 1969, ApJ, 156, 943
Taylor A. R., Gregory P. C., 1982, ApJ, 255, 210
Vilhu O., et al., 2003, A&A, 411, L405
Walborn N. R., 1973, ApJ, 179, L123
Walker E. N., 1972, MNRAS, 160, 9
Webster B. L., Murdin P., 1972, Nat, 235, 37
Wen L., Cui W., Levine A. M., Bradt H. V., 1999, ApJ, 525, 968
Whelan J. A. J., et al., 1977, MNRAS, 181, 259
Treves A., et al., 1980, ApJ, 242, 1114
Zdziarski A.A., Poutanen J., Paciesas W.S., Wen L., 2002, ApJ, 578, 357
Ziółkowski J., 2005, MNRAS, 358, 851
Zwitter T., Calvani M., D'Odorico S., 1991, A&A, 25, 92

This paper has been typeset from a TEX/ LATEX file prepared by the author.